Available online at www.sciencedirect.com
ScienceDirect
Journal of Power Sources 171 (2007) 706–717
JOURNAL OF POWER SOURCES
www.elsevier.com/locate/jpowsour

# Determination of transport parameters for multiphase flow in porous gas diffusion electrodes using a capillary network model

B. Markicevic, A. Bazylak, N. Djilali *

*Institute for Integrated Energy Systems & Department of Mechanical Engineering, University of Victoria, Victoria, BC V8W 3P6, Canada*

Received 11 May 2007; received in revised form 6 June 2007; accepted 7 June 2007
Available online 23 June 2007

**Abstract**

The changes of relative permeability and capillary pressure as a function of liquid water phase saturation, two key parameters in two-phase PEMFC models, are investigated using a capillary network model incorporating an invasion percolation algorithm with trapping. The two-dimensional capillary network accounts for capillary dominated drainage and cluster formation. It is shown that relative permeability is constant for low saturation, but follows a power law of saturation for high saturations, with an exponent of about 2.4 that is independent of network size or heterogeneity. An increase of the network size and reduction in heterogeneity tend to reduce the relative permeability, and relative permeabilities of much less then unity are obtained even for saturations as large as 0.8. Capillary pressure on the other hand does not vary with saturation and network size, but is influenced by heterogeneity only. This suggests that regardless of the interface shape and size, the capillaries at the interface maintain a constant average radius causing the capillary pressure to remain constant. It is finally shown that with appropriate scaling and for a given network heterogeneity, the normalized capillary pressure, single-phase permeability and relative permeability can be deduced for other choices of porous medium physical scales without requiring a new set of simulations.


*Keywords:* PEM fuel cell; Liquid water transport; Gas diffusion layer; Relative permeability; Capillary pressure function; Saturation

## 1. Introduction

The transport and accumulation of liquid water is a pacing item in PEM fuel cells from the view point of design and operation, and gives rise to a variety of challenging multiphase flow regimes, which are still not well characterized or understood. In this paper we focus on the multiphase flow in the porous gas diffusion layer of PEM fuel cells. Recent experimental attempts to shed light on two-phase flow in PEM fuel cells have been made by Tüber et al. [1], Nam and Kaviany [2], Pekula et al. [3], Litster et al. [4], and Bazylak et al. [5] using visualization techniques and neutron imaging, but there has been little progress in quantifying the processes. A variety of modeling strategies have been proposed (see review in Litster and Djilali [6]) to predict phase saturation in the gas diffusion layers, including the multi-fluid model (Berning and Djilali [7]) and the mixture model [8,9]. A critical aspect of these models is the need to prescribe the relative permeabilities ($k_{r,i}$) of each phase and a constitutive relation for capillary pressure ($p_c$) as a function of saturation ($s$). Remarkably, multiphase fuel cell models to date have had to rely on empirical correlations obtained from soil and sand samples. Gas diffusion layers have, as shown in Fig. 1, a radically different structure, and they are also treated to impart hydrophobicity in order to promote water transport. The effective relative permeability and capillary pressure curves are expected to be quite different [6]. In this paper we propose to address this issue using capillary pore network simulations.

There is a rich literature on multiphase flows in porous media due to their relevance in a large number of engineering applications ranging from oil recovery, chemical reactors and heat exchangers, to drainage and drying of soils. Continuum multiphase models are limited in their ability to predict surface heat and mass transfer coefficients, distribution of phases (phase saturation), and the formation of "dry patches" [10]. Discrete pore network models provide an alternative approach to elucidate transfer phenomena and to evaluate transfer parameters. In network models, an actual porous medium is represented as a network of pores that are connected by throats [11], and

* Corresponding author. Tel.: +1 250 721 6034; fax: +1 250 721 6323.
*E-mail address:* ndjilali@uvic.ca (N. Djilali).

0378-7753/$ – see front matter © 2007 Elsevier B.V. All rights reserved.
doi:10.1016/j.jpowsour.2007.06.053

**Nomenclature**

| | |
|---|---|
| **A** | system matrix |
| $A, B, \alpha, \beta, n$ | power law parameters |
| **b** | force vector |
| **D** | tri-diagonal matrix |
| $f$ | fraction of throats invaded at the outlet boundary |
| g | throat conductance ($m^3\ Pa^{-1}\ s^{-1}$) |
| $k_{r,i}$ | relative permeability |
| $K$ | permeability ($m^2$) |
| $K_{sp}$ | single-phase permeability ($m^2$) |
| $l$ | throat length (m) |
| $L$ | medium length (m) |
| $n_L$ | network size |
| $N$ | number of random network realizations |
| $p$ | pressure (Pa) |
| $\Delta p/L$ | pressure drop ($Pa\ m^{-1}$) |
| $p_c$ | capillary pressure (Pa) |
| $q$ | flow rate through one throat ($m^3\ s^{-1}$) |
| $Q$ | flow rate ($m^3\ s^{-1}$) |
| $r$ | radius (m) |
| **R** | diagonal matrix |
| $s$ | phase saturation |
| $V$ | volume ($m^3$) |
| $V_p$ | volume of pores ($m^3$) |
| $W$ | medium width (m) |
| $W \times \delta$ | medium cross-section area ($m^2$) |

*Greek letters*

| | |
|---|---|
| $\chi$ | network heterogeneity, $r_{max}/r_{min} - 1$ |
| $\delta$ | medium depth (third dimension) (m) |
| $\phi$ | porosity |
| $\mu$ | dynamic viscosity (Pa s) |
| $\sigma$ | surface tension (Pa m) |

*Subscripts*

| | |
|---|---|
| av | average |
| bt | breakthrough point, $f = 1/n_L$ |
| H | horizontal |
| inl | inlet |
| I | fluid phase |
| nex | next |
| out | outlet |
| p | pore |
| pre | previous |
| sp | single-phase |
| t | throat |
| tp | terminal point, $f = 1$ |
| V | vertical |

such models have been used to investigate a number of different processes, including two-dimensional creeping flow [12], evaporation and drainage [13–17], diffusion and dispersion [18–20], and flow in fractures [21].

A number of parameters are required for initial network definition, which include coordination number, network heterogeneity, pore and throat shape. The coordination number (connectivity) is equal to the ratio of connected pores to the site pore. For regular networks, the coordination number is equal to four and six for 2D and 3D networks, and a value of around four has been reported for 3D simulations of stochastic media [22]. In direct measurements of porous structures using microtomography, similar coordination numbers were found; although coordination numbers up to fifteen have been reported [22,23]. Another parameter defining the network heterogeneity is the size distribution of the pores and throats. Random distributions have been used with different distribution laws: beta [24], uniform, and normal [25]. In addition, the shape and cross-sectional area of the pores and throats can be different [26]. Finally, all these parameters influence the distribution of the phases in the network and interfacial area [27].

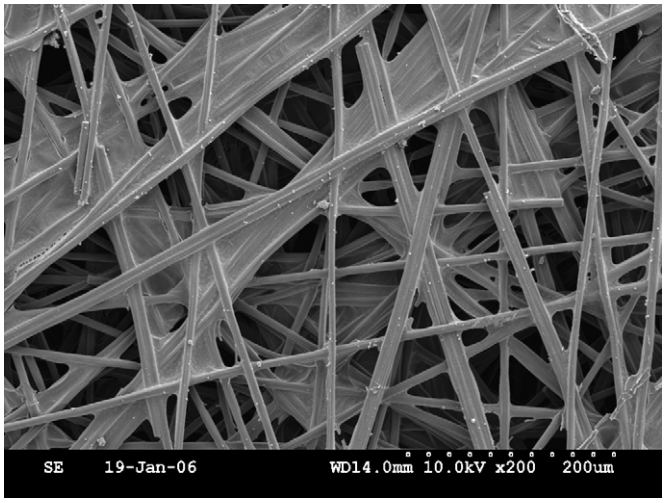


Fig. 1. Scanning electron microscope of a GDL illustrating random fibre structure and PTFE webbing.

The multiphase flow parameters (relative permeability, capillary pressure) depend on the porous medium properties, and consequently, network topology [28]. The multiphase parameters also depend on the type of process, and the predominance of gravity, viscous or capillary forces [29]. For very slow processes in which capillary forces dominate, the process follows invasion percolation [30], for which the problem formulation was proposed by Wilkinson and Willemsen [31]. The definition of the overall potential for any combination of these three forces and how the phases distribute within a porous medium is discussed in Prat [32] for all other cases. The relative influence of the three forces is characterized by the capillary and the Bond numbers [13], from which correlation length (average size of immobile fluid clusters) can be calculated [33]. The relative permeability is constant when the correlation length is much smaller than the domain size. Otherwise, when the domain is small compared to the correlation length, the relative permeability follows a power law of domain size [34].

So far the only attempt to apply pore network models to fuel cell gas diffusion media is the work of Nam and Kaviany [2] who used this method to determine the effective diffusion coefficient as a function of porosity and saturation. However, in order to compute the required water saturation profile, Nam and

Kaviany relied on the prescription of a cubic variation of the relative permeability ($k_{r,i}$) with saturation in conjunction with the Leverett function for the capillary pressure ($p_c$). The main objective of this work is to use network simulations to establish the functional dependence of the relative permeability ($k_{r,i}$) and capillary pressure ($p_c$) on the saturation ($s$) of an invading phase (liquid water), particularly in the context of fuel cell gas diffusion electrodes. The determination of such constitutive relations is a central issue in the development of reliable models for PEM fuel cells where two-phase flow conditions are commonly encountered [6,7]. In this work, the focus is on the influence of the GDL/porous medium domain properties, such as heterogeneity and layer thickness, on ($k_{r,i}$) and ($p_c$) in the limit of the capillary dominated flow (slow flows).

## 2. Capillary network model

The two main macroscopic properties used to define a porous medium are porosity ($\phi$) and permeability ($K_{sp}$), and these can be interpreted as storage and momentum transfer properties, respectively. Capillary network models exploit these in representing the medium as a network of pores and throats. The fluids are stored in the pores, where there is no resistance to transfer between phases, whereas the transfer resistance is associated with the throats, defined as volumeless connections between the pores. A schematic of such a two-dimensional network with each pore connected to four throats is depicted in Fig. 2. In order to investigate fluid flow through a specific porous medium using a network model, the macroscopic parameters have to be adjusted appropriately. Hence, the capillary network is defined such that the total volume of pores ($V_p$) is equal to the void volume of the porous medium. Normalizing with the overall volume of the porous medium ($V$), the porosity is obtained:

$$\phi = \sum_i \frac{V_{p,i}}{V} \tag{1}$$

Similarly, the permeability of the network is set by adjusting the throats appropriately. In single-phase flow through either a porous medium or network, Darcy's law applies. Given a pressure drop ($(p_{inl} - p_{out})/L$) across the network, and a flow rate ($Q$) through a network boundary of area ($W \times \delta$), the single-phase permeability is defined as,

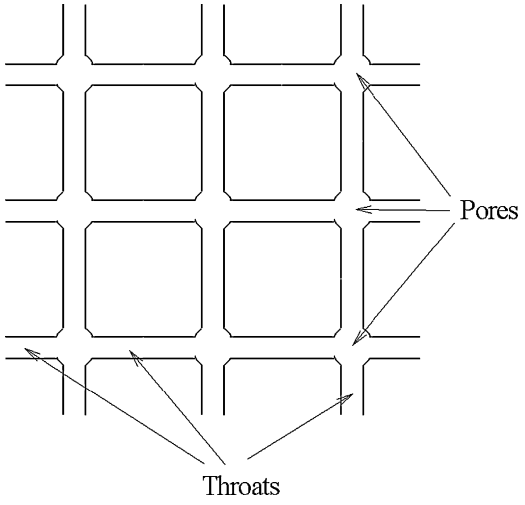


Fig. 2. Porous medium representation as a network consisting of pores and throats.

$$K_{sp} = \mu \frac{L}{p_{inl} - P_{out}} \frac{Q}{W\delta} \tag{2}$$

where ($\mu$) is the fluid viscosity. Since the network is a heterogeneous medium, the single-phase permeability ($K_{sp}$) is an effective permeability that decreases as the medium becomes more heterogeneous [35,36]. Hence, the variation of the single-phase permeability can be used as an additional constraint to bound pore and throat distribution laws.

The other important issue is how storage and transport quantities (porosity and permeability) are altered due to the presence of multiphase flow. In multiphase systems, because transfer resistances and potentials differ, the phase with the lower potential is displaced (replaced) by other phase(s) whose potential is higher. Thus, the void volume is occupied with two or more phases, and in order to quantify phase content, the phase saturation is defined. When two or more phases are present, the transport of each phase is reduced compared to single-phase flow. Thus, the phase permeability ($K_i$) needs to be calculated with respect to each phase. To do so, the laws for single-phase flow are assumed to be valid in multiphase flow. For the momentum transfer corresponding to each phase ($i$), the Darcy law relates the phase velocity vector ($\mathbf{u}_i$) and the phase pressure gradient ($\nabla p_i$):

$$\mathbf{u}_i = -\frac{K_i}{\mu_i} \nabla p_i \tag{3}$$

where ($i = 1, \ldots, n_p$) and ($n_p$) is the number of phases. Using Eq. (3), the definition of a phase is preserved; this corresponds to a part of the domain having different properties than the remaining parts. Here, the viscosity ($\mu_i$) of the fluid is distinct for each phase. Furthermore, given the distribution of each phase, the phase parameters for a multiphase system can be calculated. The network models can readily be used for such calculations, since it is straightforward to obtain the saturation of each phase in the overall medium.

In Eq. (3), the phase permeability ($K_i$) accounts for the presence of both porous media and content of other phases (saturation), whereas the single-phase permeability ($K_{sp}$) represents the influence of the porous medium. In order to obtain a permeability that accounts for the influence of the saturation only, the relative permeability ($k_{r,i}$) is defined as a ratio of these two permeabilities:

$$k_{r,i} = \frac{K_i}{K_{sp}} = \left(\frac{Q_i}{\Delta p_i / L_i}\right)\left(\frac{\Delta p / L}{Q}\right) \tag{4}$$

where ($\Delta p_i/L_i$) is the pressure drop for an individual phase in multiphase flow, and is generally different from the single-phase pressure drop ($\Delta p/L$). Thus, Eq. (4) implies that the pressure field can change due to the presence of multiple phases thereby altering ($k_{r,i}$).

Since two phases coexist, a condition at the interface(s) between the phases has to be included. In general, a pressure difference ($p_i - p_j$) arises between phases ($i$) and ($j$) at the interface,

i.e. the capillary pressure. As a criterion for phase displacement, the pressure difference is compared to the threshold capillary pressure ($p_c$), which can be calculated from the Young–Laplace equation:

$$p_c = \frac{2\sigma}{r_t} \tag{5}$$

where ($\sigma$) is the surface tension and ($r_t$) is the radius of capillary. For very slow processes (capillary dominated), a simpler displacement criterion can be used, i.e. the throat with the largest radius at the interface will be invaded by invading fluid. The invaded fluid can be trapped in the network (clusters) if the invading fluid flow paths merge, form internal loops, or hit the no-flow network side. Furthermore, the throat invasion is quasi-static, meaning that each throat can be invaded at most once, and therefore the invading phase pattern is a static configuration as well. This process is referred as invasion percolation with trapping, as defined in Wilkinson and Willemsen [31], and processes such as slow drainage follow this pattern.

Usually, the invasion is stopped once the invading fluid appears at the outlet boundary, where only one outlet throat is invaded. This is the breakthrough point of the process. However, the invasion can be stopped anytime between breakthrough and when all throats at the outlet are invaded (the terminal point). The fraction of invaded throats at the outlet ($f$) is therefore ($f = 1/n_L$) and ($f = 1$) for breakthrough and the terminal points, respectively. We distinguish two types of invading fluid flow paths: (i) the flow paths that connect the network inlet and outlet, (ii) and the flow paths that do not reach the network outlet, as they become part of invaded fluid clusters. The invading fluid carrying backbone comprises all connecting flow paths, and only this part of the invading phase contributes to the momentum transfer. The variation of the invading fluid flow paths pattern is caused by: (i) invasion stopping point, and (ii) network randomness. Using this framework, we investigate how multiphase parameters vary with invading phase saturation.

## 3. Numerical procedure

We define a regular square capillary network of size ($n_L \times n_L$) with randomly generated throat radii. The invading fluid enters the network at one side (inlet) and the invaded fluid flows out of the opposite side of the network (outlet). There is no flow through the other two network sides. In a sequence of discrete steps, the invading fluid occupies the throat with the lowest potential (largest throat radius) at the interface. Thus, the interface moves and the flow paths of invading fluid expand. The invading fluid pattern for a particular network realization is not affected significantly by an invasion stopping point (between breakthrough and terminal points), as the flow pattern is already developed in the breakthrough point. However, the patterns of flow paths and clusters can be very different for distinct random realizations that might cause large variations in multiphase flow parameters. Two limiting cases are (i) a network with very large cluster size, for which flow paths are less branched, and (ii) the opposite case of a network with small clusters and highly branched flow paths. Fig. 3(a and b) illustrate these

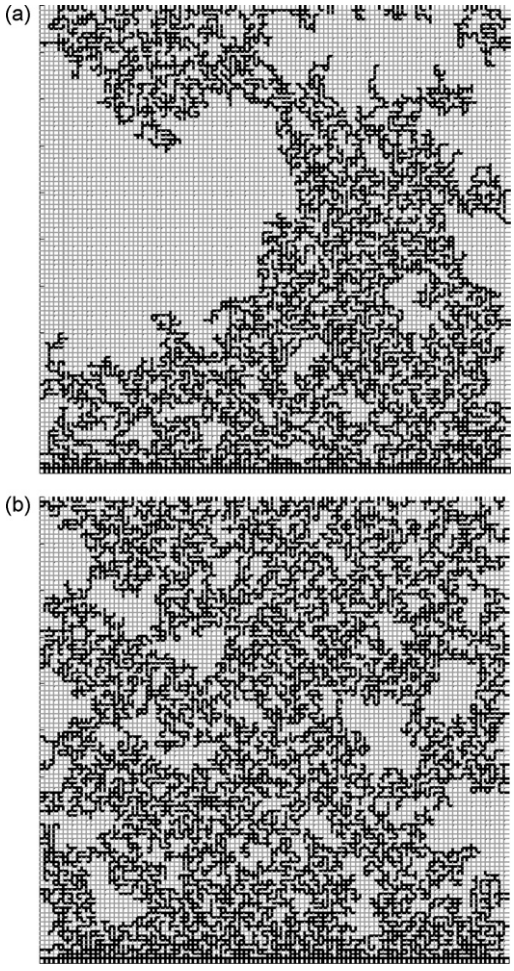


Fig. 3. Invasion of a capillary network for cases of (a) low saturation, and (b) high saturation of invading phase. The inlet and outlet are located at the top and bottom of the network boundary, respectively.

two limiting cases in which invading and invaded phases are shown with thick black and gray lines, respectively. Here, the fluid enters the network at the top boundary, and the outlet boundary is at the bottom of the network. Corresponding carrying backbones of the case depicted in Fig. 3(b) is shown in Fig. 4.

In order to calculate the single-phase ($K_{sp}$) and the invading phase permeability ($K_i$) (see Eq. (2) for single-phase permeability), the pressure solutions within the network (for $K_{sp}$) and the carrying backbone (for $K_i$) are required. This is obtained from the simultaneous solution of the material balance equations over all pores within the network/backbone. For each pore in the network/backbone and corresponding throats, the overall material balance can be written in the form:

$$\sum_{j=1}^{c} q_j = 0, \quad c = 4 \tag{6}$$

where ($c$) is the coordination number; in single-phase flow this represents the number of throats belonging to each pore (equal to four for regular square 2D network). In multiphase flow, because the backbone is defined as a static configuration with no phase transport across an interface, the coordination number for the

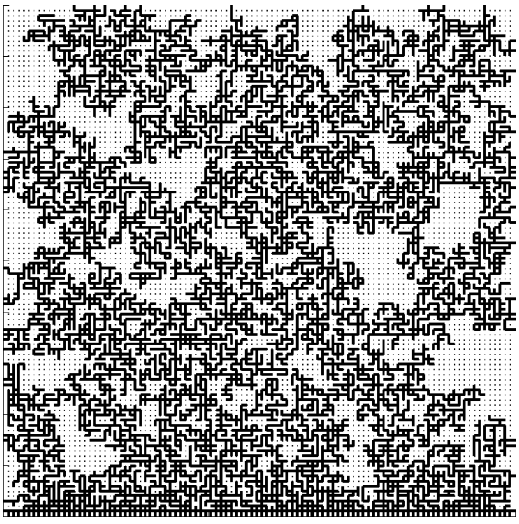

Fig. 4. Carrying backbone formed for case of high saturation of invading phase.

pores at the interface is smaller than four since at least one throat is occupied by the invaded fluid.

The material balance for one throat is given by the flow rate ($q_j$) through the throat and is calculated from the throat conductance ($g_j$) and the pressure difference ($\Delta p$) between the starting and ending pores of the throat:

$$q_j = g_j\,\Delta p \tag{7}$$

where the throat is treated as a capillary of radius ($r_t$) and length ($l$) occupied by one phase of viscosity ($\mu$). The conductance is obtained from Poiseuille's law:

$$g_j = \frac{\pi r_t^4}{8\mu l} \tag{8}$$

In Fig. 5, a pore $(i, j)$ and four connecting throats $(i-1, j)$, $(i+1, j)$, $(i, j-1)$ and $(i, j+1)$ are depicted. Both horizontal (H) and vertical (V) throats can be *previous* (pre) or *next* (nex) to the pore $(i, j)$. Since the direction of the flow for each throat is not known *a priori*, all $(q_j)$ are defined as flow into $(i, j)$ pore. Using this convention and Eq. (6), the material balance and from there

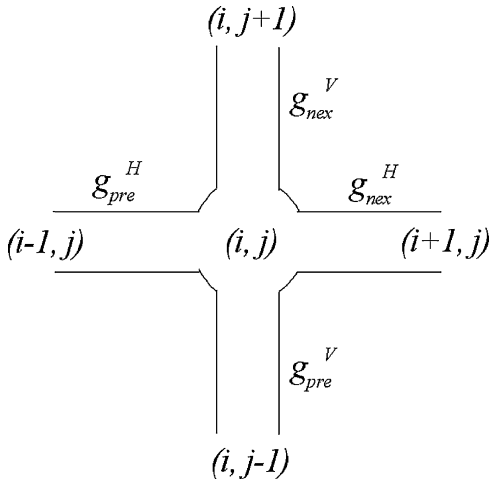


Fig. 5. Network node with one pore and connecting throats.

the pressure balance for pore $(i, j)$ obeys:

$$g^{\mathrm{H}}_{\mathrm{pre}}p_{-10} + g^{\mathrm{H}}_{\mathrm{nex}}p_{+10} + g^{\mathrm{V}}_{\mathrm{pre}}p_{-01} + g^{\mathrm{V}}_{\mathrm{nex}}p_{+01} - (g^{\mathrm{H}}_{\mathrm{pre}} + g^{\mathrm{H}}_{\mathrm{nex}} + g^{\mathrm{V}}_{\mathrm{pre}} + g^{\mathrm{V}}_{\mathrm{nex}})p_{00} = 0 \tag{9}$$

where the subscripts for pressure ($p$), flow rate ($q$) and conductance ($g$) are with reference to Fig. 5. An expression of a similar form to Eq. (9) can be obtained for a pore at the interface that belongs to the carrying backbone, where the throats with invaded fluid are omitted as they do not contribute to the balance of the invading phase. Applying Eq. (9) to each pore yields a linear system of algebraic equations for pressure (**p**):

$$\mathbf{A}\,\mathbf{p} = \mathbf{b} \tag{10}$$

The vector (**b**) depends on the pressure boundary conditions, and is assembled using Eq. (9) with specified pressures at the inlet and outlet of the network. Matrix (**A**) is a typical finite difference matrix and for a network of $(n_L \times n_L = n_L^2)$ pores, it has a block-matrix form:

$$A = \begin{bmatrix} R_{1,1} & D_{1,2} & 0 & \dots & 0 & 0 & 0 \\ D_{2,1} & R_{2,2} & D_{2,3} & \dots & 0 & 0 & 0 \\ 0 & D_{3,1} & R_{3,3} & \dots & 0 & 0 & 0 \\ \vdots & \vdots & \vdots & \vdots & \vdots & \vdots & \vdots \\ 0 & 0 & 0 & \dots & R_{n-2,n-2} & D_{n-2,n-1} & 0 \\ 0 & 0 & 0 & \dots & D_{n-1,n-2} & R_{n-1,n-1} & D_{n-1,n} \\ 0 & 0 & 0 & \dots & 0 & D_{n,n-1} & R_{n,n} \end{bmatrix} \tag{11}$$

where matrices (**R**) and (**D**) are tri-diagonal and diagonal, respectively, with conductance of throats incorporated from Eq. (9):

$$R_{ii} = \mathrm{tridiag}(g^{\mathrm{H}}_{\mathrm{pre},i}, -g^{\mathrm{H}}_{\mathrm{pre},i} - g^{\mathrm{H}}_{\mathrm{nex},i} - g^{\mathrm{V}}_{\mathrm{pre},i} - g^{\mathrm{V}}_{\mathrm{nex},i}, g^{\mathrm{H}}_{\mathrm{nex},i}) \tag{12}$$

$$D_{ij} = \mathrm{diag}(g^{\mathrm{V}}_{\mathrm{pre},i}\,(i < j), g^{\mathrm{V}}_{\mathrm{nex},i}\,(i > j)) \tag{13}$$

Matrix (**A**) is a sparse matrix with a scarcity of approximately $1/n_L^2$. Using sparse matrix solvers for a network of $n_L \times n_L = 100 \times 100$ (matrix (**A**) has $10^8$ elements out of which $10^4$ are non-zero), the inversion of (**A**) can be obtained in a few seconds (MatLab package). Eq. (11) can be readily extended to 3D networks and networks with variable coordination number.

A typical pressure profile for the carrying backbones (Fig. 4) of the invading fluid is depicted in Fig. 6. The pressure drop is not constant, and the influence of network edges (inlet and outlet) is clearly illustrated. As the invading fluid meanders along paths with less flow resistance, the pressure changes are different in the middle part of the network than at the edges. Averaging the pressure along a direction perpendicular to the flow, an averaged pressure profile along the flow direction is calculated and shown in Fig. 7 for four different invasion stopping points: breakthrough ($f = 1/n_L$), terminal ($f = 1$), and two points ($f_1$) and ($f_2$) ($1/n_L < f_1 < f_2 < 1$), where ($f$) is a fraction of invaded throats at the outlet. Fig. 7 also depicts the pressure drop in the middle part of network that is caused by the presence of two-phases (cf. Eq. (4) and how relative permeability is calculated). Clearly, the pressure drop depends on the stopping point ($f$).

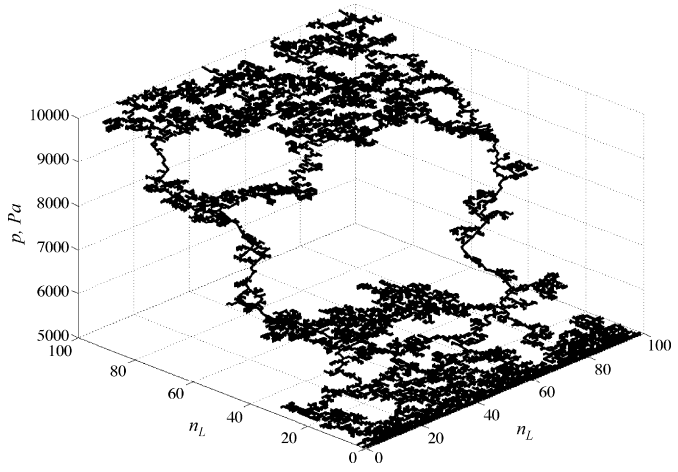


Fig. 6. Calculated pressure profile in the carrying backbone.

## 4. Results and discussion

The simulations are performed using a regular square network of ($n_L \times n_L$) pores with coordination number equal to four. Five network sizes were used $n_L = \{20, 40, 60, 80, 100\}$. A network consists of a total of $2n_L(n_L + 1)$ cylindrical throats of dimension ($r$, $l$), and each throat is occupied by one phase only (either invading or invaded fluid). The length of the throat was set to ($l = 2 \times 10^{-3}$ m). To account for the porous medium heterogeneity, the throat radius was initially set as a random variable, with an average radius $r_{av} = 4 \times 10^{-4}$ m. The radii ($r$) are uniformly distributed in range ($r_{min}$, $r_{max}$) $\times 10^{-4}$m with ($r_{min}$, $r_{max}$) = {(3.5, 4.5), (2, 6), (1, 7), (0.5, 7.5), (0.2, 7.8)} and a heterogeneity parameter defined as ($\chi = r_{max}/r_{min} - 1$); thus $\chi = \{0.3, 2, 6, 14, 38\}$. For each particular combination ($n_L$, $\chi$), $N = 100$ network realizations with randomly generated ($r$) are obtained, and from these we calculate average parameters. Using the above values of ($r_{av}$, $l$), a single-phase permeability of order $10^{-9}$ m$^2$ is obtained; whereas for a typical gas diffusion layer ($K_{sp}$) is in the order of $10^{-12}$ m$^2$. Scale analysis can be used to adjust the network parameters to achieve the required permeability. In a network, the single-phase permeability is proportional to $r_{av}^4/l$ and for two networks having the same heterogeneity parameter ($\chi$), the group $K_{sp} \times l/r_{av}^4$ should be the same irrespective on the values ($r_{av}$, $l$). The same scaling applies for the phase permeability ($K_i$), and therefore, the relative permeability should be a function of the heterogeneity parameter ($\chi$) only, and should not depend on ($r_{av}$, $l$). The capillary pressure ($p_c$) is also expected to vary proportionally with the inverse of the throat radii at the interface ($1/r$), and the group ($p_c \times r_{av}$) should thus produce the same results regardless of the value ($r_{av}$) as long as ($\chi$) is kept constant. In order to verify the validity of the scaling arguments, the numerical simulations are repeated for the network $n_L = 60$, but with $r_{av} = 4 \times 10^{-5}$ m, a value close to those observed in GDLs, and $l = 2 \times 10^{-4}$ m and all five $\chi = \{0.3, 2, 6, 14, 38\}$. Using these values of ($r_{av}$, $l$), yields ($K_{sp}$) values that are three orders of magnitude lower (i.e. $10^{-12}$ m$^2$), and ($p_c$) values an order of magnitude higher. The relative permeability should stay unchanged, and this will be discussed in Section 4.2.

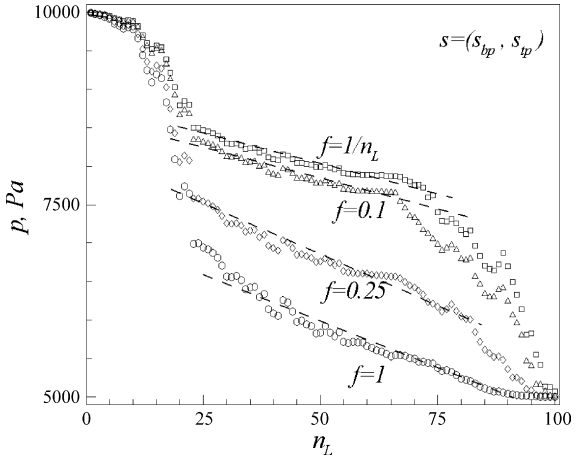


Fig. 7. Averaged (direction perpendicular to the fluid flow) pressure profiles along the fluid flow direction for different fraction of invaded throats at the outlet ($f$). The pressure drop in the multiphase region is also shown (dashed lines).

The invasion percolation algorithm with trapping is used to obtain invading phase distribution into the invaded phase, where the invasion is stopped in the range from the breakthrough (one throat at the outlet is invaded) to the terminal point (all throats at the outlet are invaded). For a known phase distribution, the invading phase saturation ($s$), single-phase ($K_{sp}$), invading phase ($K_i$), invading phase relative permeability ($k_{r,i} = K_i/K_{sp}$), and capillary pressure ($p_c$) are calculated. From the pressure solution (see Fig. 7), it can be observed that the pressure changes linearly in the middle part of the network, where all parameters ($s$, $K_{sp}$, $K_i$, $k_{r,i}$, $p_c$) are calculated. The saturation ($s$) is calculated based on the number of pores occupied by invading phase and overall number of pores, whereas permeabilities are obtained from the computed pressure and the phase flow rate in the network (Eqs. (2) and (4)). Throughout the network, continuity is satisfied and the flow rate is constant and equal to the flow rate at the inlet and outlet of the network. Finally, the capillary pressure ($p_c$) is found by averaging the capillary condition (Eq. (5)) at the backbone interface.

For one network random realization, stopping the invasion in the range from breakthrough ($f = 1/n_L$) to the terminal point ($f = 1$), where we recall ($f$) is the fraction of the invaded throats at the outlet, we obtain the invading phase saturation range $s = (s_{bp}, s_{tp})$. This range changes for distinct random realizations ($N$). Overall, there is an inherently large scatter in the saturations obtained from the various realizations (these correspond to the local variations in the water content in the GDL). The scatter is influenced by both stopping point $f = (1/n_L, 1)$ and random realization, and is dominated by the latter. Furthermore, the network size ($n_L$) influences the saturation scatter. For each ($n_L$), we calculate the average saturation ($s_{av}$) for ($N = 100$) and correlate this value with ($n_L$) for particular ($f$), or for all ($f$). The log–log ($s_{av}$–$n_L$) plots are shown in Fig. 8, where ($f$) is given as a parameter. Wilkinson and Willemsen [31] have shown that ($s_{av}$–$n_L$) follows a power law:

$$s_{av} = A_s n_L^{-\alpha} \tag{14}$$

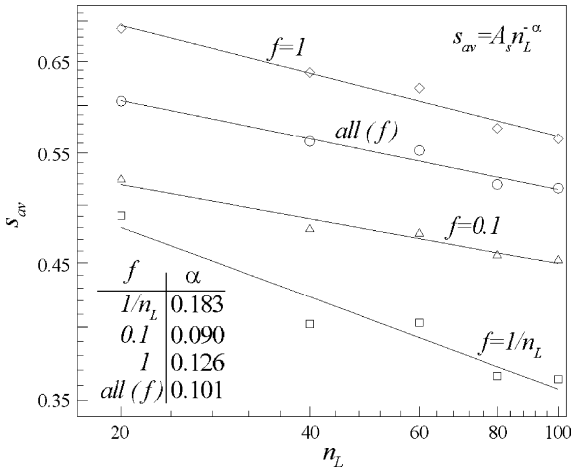


Fig. 8. Dependence of the average saturation (averaged over $\Delta s = 1.0$) on the network size ($n_L$) for different fractions of invaded throats at the outlet ($f$).

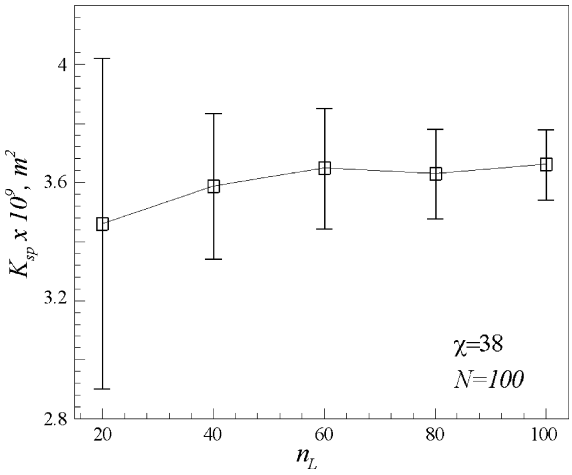


Fig. 9. Influence of network size ($n_L$) on single-phase permeability.

where the exponent ($\alpha$) for invasion percolation with trapping is ($\alpha = 0.18$). In our case this corresponds to the stopping in the breakthrough point ($s = s_{bp}$, $f = 1/n_L$), where we found ($\alpha = 0.183$). As we proceed toward ($s = s_{tp}$, $f = 1$), ($\alpha$) decreases and approaches ($\alpha = 0.10$), which is close to the percolation exponent ($\alpha = 0.12$). For ($s$) averaged for all ($f$), we found ($\alpha = 0.101$). Ultimately, we find that the distribution of ($s$) does not depend on the heterogeneity ($\chi$), as spreading of the invading fluid is influenced by radius size difference rather than magnitude difference.

### 4.1. Single-phase flow

For single-phase flow, the single-phase permeability ($K_{sp}$) is computed. Since the throat radius is a random variable with a particular distribution (uniform in this study), the calculated ($K_{sp}$) is an effective permeability for which it is assumed that Darcy's law applies. The influence of both ($n_L$) and ($\chi$) on ($K_{sp}$) is investigated. Providing that the network is stochastically homogeneous (sufficiently large), an average of ($K_{sp}$) should not depend on ($n_L$) (see, e.g. [35,36]), as moments of the throats distribution function remain the same. The deviation of ($K_{sp}$) is expected to decrease as a function of ($n_L$), as the number of throats increase with ($n_L$). The results of calculations for ($K_{sp} \sim n_L$) are summarized in Fig. 9, where the average ($K_{sp}$) and deviation are shown with symbols and error bars, respectively. For ($n_L \geq 40$), the average ($K_{sp}$) becomes essentially constant.

As the medium heterogeneity is quantified by the throat distribution moments, the effective permeability decreases as the porous medium becomes more heterogeneous (see, e.g. [36]). According to Katz and Thompson [37], ($K_{sp}$) is proportional to the characteristic length. The characteristic length is defined with respect to some threshold (capillary pressure) in which an infinite cluster is formed, and this characteristic length decreases as medium heterogeneity increases, and thus ($K_{sp}$) decreases with ($\chi$). This implies that ($K_{sp}$) is the largest for homogeneous porous media (the corresponding network would consist of throats of equal size). It should be noted here that the permeability of a porous medium is generally at least a two-parameter function; in the Kozeny equation the two parameters used are medium porosity and hydraulic diameter. Katz and Thompson [37] showed that the permeability can also be expressed as a function of formation factor and a characteristic length without an explicit dependence on porosity. Similarly, pore network simulations appear to yield single-phase permeabilities that are independent of porosity, but it should be kept in mind that a network is constructed such that its momentum transport resistance is the same as that of the actual medium. In this work, two parameters are again used ($r_{av}$, $l$) and these are adjusted to achieve the same ($K_{sp}$) as the porous medium. However, for *distinct* network realizations, there is a variation in ($K_{sp}$). The variation of ($K_{sp}$) for $N = 100$ random realizations is shown in Fig. 10 for five different ($\chi$) and $n_L = 60$. For a network that is nearly homogeneous ($\chi \approx 0.3$), the variation in ($K_{sp}$) is minimal. As ($\chi$) increases, a larger variation in ($K_{sp}$) can be observed, and furthermore the average ($K_{sp}$) decreases as depicted in the inset figure ($K_{sp} \sim \chi$). In Fig. 10, single-phase permeability is plotted

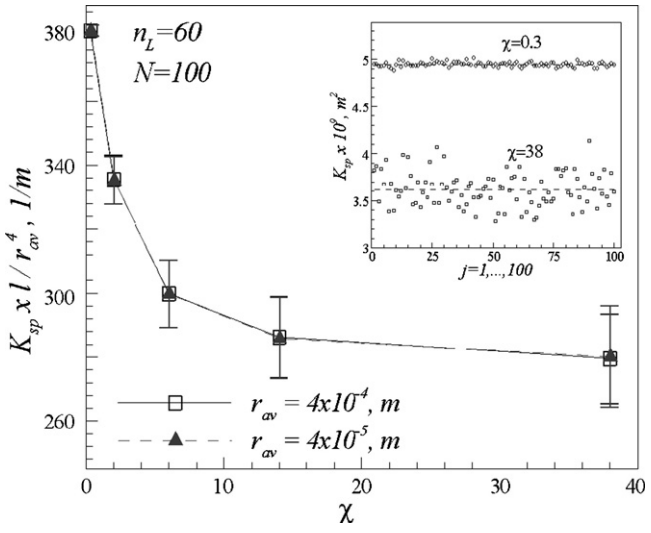


Fig. 10. Variations of the single-phase permeability as a function of the heterogeneity parameter for ($n_L = 60$). Inset figure shows ($N = 100$) realizations for ($\chi = 2$) and ($\chi = 38$). Calculations performed for $r_{av} = 4 \times 10^{-4}$ and $4 \times 10^{-5}$ m.

in terms of the group $K_{sp} \times l/r_{av}^4$, with open and filled symbols representing results for $r_{av} = 4 \times 10^{-4}$ m and $r_{av} = 4 \times 10^{-5}$ m, respectively. The results demonstrate that scaling by $l/r_{av}^4$ does indeed collapse the ($K_{sp}$) results on a single curve as long as the heterogeneity parameter is kept constant. The changes in the average value and variability of ($K_{sp}$) also influence the value and variability of the computed relative permeability ($k_{r,i}$) examined next.

### 4.2. Relative permeability

Like saturation ($s$), the relative permeability of the invading phase ($k_{r,i}$) depends on the network size ($n_L$) and fraction of throats invaded at the outlet boundary ($f$), and there is some ($k_{r,i}$) scatter caused by varying stopping points (from breakthrough to terminal point) and random network configurations. In the context of a gas diffusion layer, the stopping point is particularly important due to the presence of the collector plate land area; it is only once the liquid water reaches the outlet boundary under the channel area that liquid water flow occurs. Regardless of the set value of ($f$), the average of ($k_{r,i}$) decreases with increasing ($n_L$). Correlating averaged ($k_{r,i}$) and ($n_L$) for a particular ($f$) we find that the power law applies:

$$(k_{r,i}) = A_k n_L^{-\beta} \tag{15}$$

with the exponent ($\beta = 1.08$) for breakthrough point ($f = 1/n_L$) and ($\beta = 0.914$) for terminal point ($f = 1$). Finally, for all ($f$) a value of ($\beta = 0.910$) is found. These results are shown in Fig. 11(a). In Eq. (15), we choose ($f$) and then average the relative permeability of invading phase ($k_{r,i}$) for all random ($k_{r,i}$) irrespective of ($s$) (this provides a saturation window of $\Delta s = 1.0$). From there we deduce the exponent ($\beta$). In order to check whether ($\beta$) depend on saturation ($s$), we correlate the average ($k_{r,i}$) with ($n_L$) for a saturation window ($\Delta s < 1.0$). Average ($k_{r,i}$) versus saturation ($s$) is plotted in Fig. 11(b), showing a power law dependence of ($k_{r,i} \sim n_L$) with an exponent ($\beta$) that decreases with ($s$) (in this study from 1.05 to 0.719). For low ($s$), ($\beta$) is close to the value obtained for ($\Delta s = 1.0$), whereas for high ($s$) there is a large decrease in ($\beta$).

Variations in: (i) network size ($n_L$), (ii) stopping point ($s_{bt} \le s \le s_{tp}$), and (iii) network configuration (random realizations) which correspond to: (i) gas diffusion layer thickness, (ii) shoulder/land width, and (iii) local variation in liquid water produced, respectively, all generate changes in ($k_{r,i}$) and ($s$). These changes are used to investigate the dependence between ($k_{r,i}$) and ($s$), with ($k_{r,i}$) taken as a configurational permeability. In any case ($k_{r,i}$) is expected to increase with saturation, and for single-phase flow ($s = 1$) it takes the value ($k_{r,i} = 1$). Fig. 12 shows how the relative permeability ($k_{r,i}$) changes with saturation ($s$) for a network size ($n_L = 100$) and a heterogeneity parameter ($\chi = r_{max}/r_{min} - 1 = 38$). Each line ($k_{r,i} \sim s$) represents one random network realization ($N = 100$) for the saturation range ($s_{bt} \le s \le s_{tp}$); for clarity only some of the ($N = 100$) realizations are shown. Due to the configuration, different cases arise from small to large changes of ($s$) that are accompanied by large or small changes of ($k_{r,i}$) (lines (a) and (b), respectively). Furthermore, both ($s$) and ($k_{r,i}$) can change significantly (line (c)) or exhibit more complex dependence (line (d)). Hence, there is a large spread of individual ($k_{r,i} \sim s$) curves due to the random configurations.

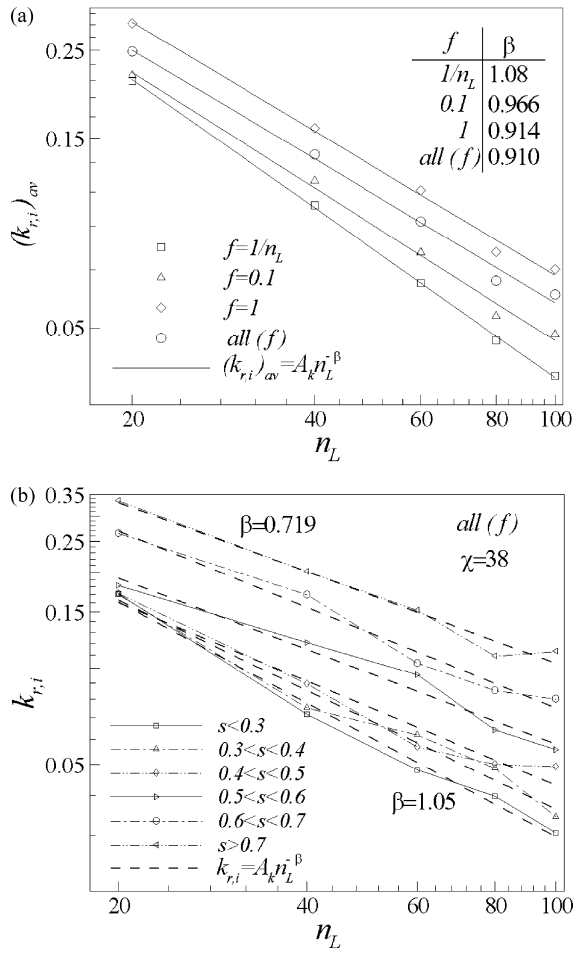


Fig. 11. Dependence of the average relative permeability on the network size ($n_L$): (a) curves averaged permeabilities over ($\Delta s = 1.0$) for different fraction of invaded throats at the outlet ($f$); (b) averaged for saturation range ($\Delta s < 1.0$).

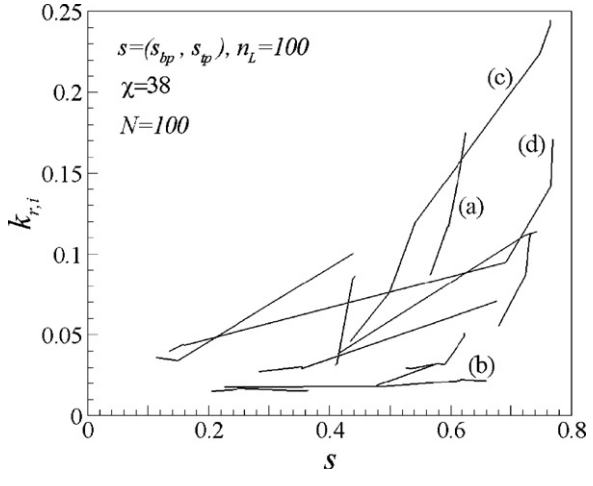


Fig. 12. Random realization tendencies of ($k_{r,i} \sim s$) curves for stopping points range between the breakthrough and the terminal point.

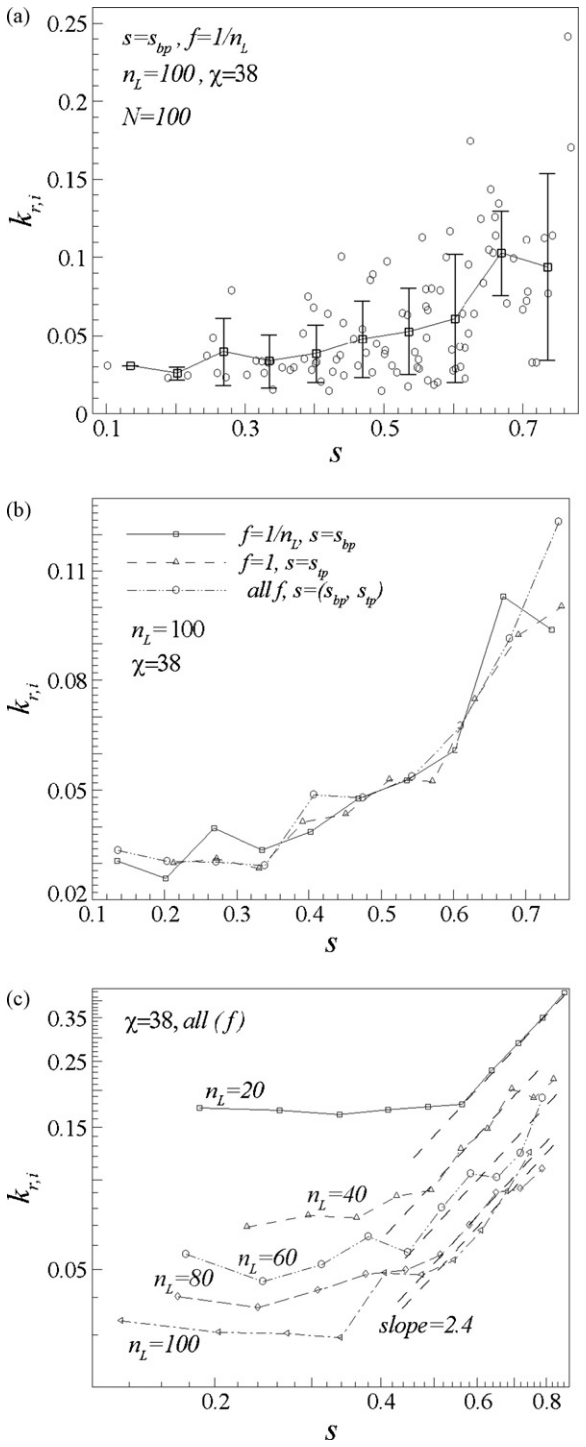


Fig. 13. Averaged values of the relative permeability ($k_{r,i}$) as a function of saturation: (a) for network random realizations ($N = 100$) and ($n_L = 100$) and ($\chi = 38$) in breakthrough point ($f = 1/n_L$), (b) curves ($k_{r,i} \sim s$) for breakthrough, terminal point and whole range ($1/n_L$, 1), (c) family of ($k_{r,i} \sim s$) curves for different ($n_L$). Dashed line (in part (c)) represents curve for power of ($n = 2.4$).

For ($n_L = 100$) and ($\chi = 38$) at breakthrough point ($f = 1/n_L$), the results for ($k_{r,i}$) and $N = 100$ random realizations are depicted with circles in Fig. 13(a). Invading phase relative permeability ($k_{r,i}$) values averaged in saturation increments (here for ten increments of $\Delta s$) are depicted with squares, and the standard deviation of ($k_{r,i}$) is shown with error bars. For low ($s$), ($k_{r,i}$) is constant and then increases for higher ($s$). The procedure of averaging ($k_{r,i}$) and ($s$) is repeated for: (i) terminal point ($f = 1$), and (ii) over all range $f = (1/n_L, 1)$. Thus, three distinct curves ($k_{r,i} \sim s$) are obtained and shown in Fig. 13(b). All curves collapse on essentially the same dependence. Using averaged curves ($k_{r,i} \sim s$) for all ($f$) (circles and double dotted line in Fig. 13(b)) we obtain a family of curves ($k_{r,i} \sim s$) for various network sizes ($n_L$) shown in Fig. 13(c). As suggested in the literature, there is a power law dependence ($k_{r,i} \sim s^n$), with the power ($n$) varying from unity to some higher values, depending on the capillary number and type of process [38]. For larger network sizes ($n_L$), ($k_{r,i} \ll 1$) even for high $s \approx 0.8$ (see Fig. 13(c)). Hence, for the non-constant part of a ($k_{r,i} \sim s$) curve, we correlate ($k_{r,i}$) as a power function of ($s$):

$$k_{r,i} = B_L s^n \tag{16a}$$

For which ($B_L$) is found to decrease with ($n_L$), and ($n$) remains constant ($n = 2.4$).

On the other hand, by altering the porous medium heterogeneity ($\chi$), there is an additional change of ($k_{r,i}$) However, assuming that ($k_{r,i}$) is still a power function of ($s$), a modified expression is adopted:

$$k_{r,i} = B_\chi s^n \tag{16b}$$

with ($n$) and ($B_\chi$) taken to depend on the parameters ($n_L$) and ($\chi$). The results for constant ($n_L = 60$) and five different ($\chi$) are presented in Fig. 14. The open symbols in Fig. 14 represent ($k_{r,i}$) results for $r_{av} = 4 \times 10^{-4}$ m, and filled symbols depict results for $r_{av} = 4 \times 10^{-5}$ m. The relative permeability shows essentially the same dependence ($k_{r,i} \sim s$) regardless of ($r_{av}$), consistent with the fact that the scaling factor $l/r_{av}^4$ is the same for both ($K_{sp}$) and ($K_i$) cancels out in the relative permeability ($k_{r,i} = K_i/K_{sp}$). As for ($n_L$), ($k_{r,i}$) is constant for low ($s$) and then increases for higher ($s$). The relative permeability increases with ($\chi$) (family of curves in Fig. 14). The parameter ($B_\chi$) increases with ($\chi$), and an approximately constant value for ($n$) of around 2.4 is found. Here, both *powers* are equal (Eqs. (16a) and (16b)), regardless of ($n_L$) and ($\chi$). However, the parameters ($B_L$) and ($B_\chi$) and ($k_{r,i}$)

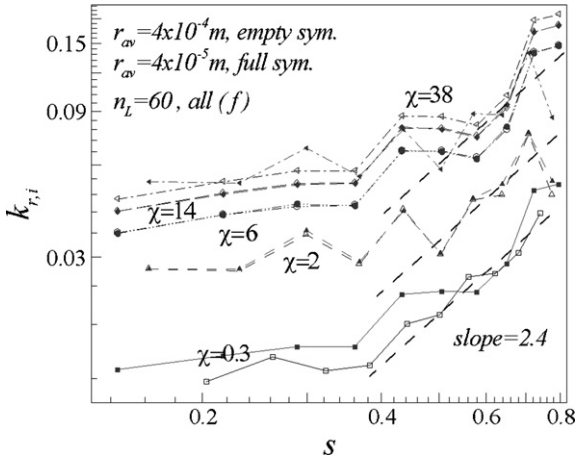


Fig. 14. Relative permeability as a function of saturation for different heterogeneity parameters. Power law fits ($n = 2.4$) are plotted with dashed lines. Calculations performed for $r_{av} = 4 \times 10^{-4}$ and $4 \times 10^{-5}$ m.

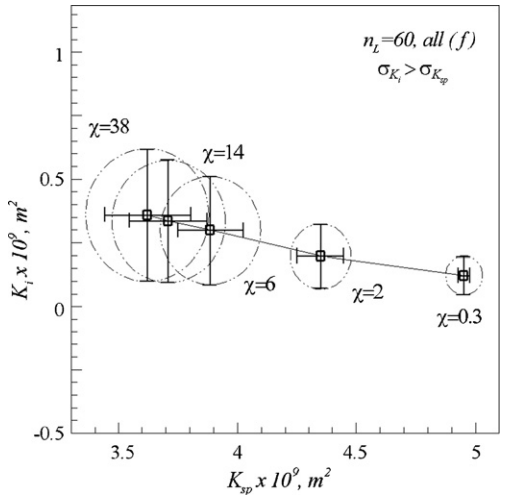


Fig. 15. Variation of single-phase permeability ($K_{sp}$) and invading phase permeability ($K_i$) for ($n_L = 60$) with different ($\chi$). Errors bars are shown for ($K_{sp}$) and ($K_i$). ($K_i$) changes more slowly and with larger variation (dash dot circles) than ($K_{sp}$).

for low ($s$) (Fig. 13 and subpart (c, left sides)) vary with ($n_L$) and ($\chi$). This confirms that it is possible to alter ($k_{r,i}$) not only with the type of process but also with the structure of the porous medium ($n_L$, $\chi$). However, as the power ($n$) remains constant, it appears that ($n$) is influenced by the capillary number (process rate) only when the correlation length is altered (here the capillary number is very low and all changes occur in the capillary regime).

The most important distinction between the single-phase permeability ($K_{sp}$) and the relative permeability ($k_{r,i}$) is that ($k_{r,i}$) increases as the heterogeneity parameter ($\chi$) increases, i.e. the opposite of the behavior of ($K_{sp}$).However, the question is how does the invading phase permeability ($K_i$) changes with ($\chi$)? This is addressed in Fig. 15, where ($K_{sp}$) and ($K_i$) are correlated for ($n_L = 60$) at five values of ($\chi$). Based on the nature of the interaction between the invading fluid and porous medium, the external pressure drives the invading fluid into the available throats with the largest radius, where the capillary pressure is smallest. Hence, as ($\chi$) increases, ($K_i$) increases as throats with invading fluid become larger, whereas ($K_{sp}$) decreases as shown in Fig. 10. The results ($K_{sp}$, $K_i$) show that ($K_i$) increases with ($\chi$) more slowly than ($K_{sp}$) decreases, but exhibits larger variations than ($K_{sp}$) (vertical error bars for ($K_i$) are larger than horizontal ones for ($K_{sp}$)). The error bars reveal a major difference between ($K_i$) and ($K_{sp}$), where the variation of ($K_i$) is influenced with configuration of the carrying backbone, thus resulting in a large variation of ($K_i$), even for small ($\chi$).

### 4.3. Capillary pressure

The capillary pressure is calculated at the same part of the capillary network as the saturation and invading phase permeability. At the invaded/invading fluid interface, the pressure difference between two neighboring pores, each belonging to two different phases (gas and water), is equal to the capillary pressure, $p_c = p_{\text{non-wetting}} - p_{\text{wetting}}$. The capillary pressure ($p_c$) is equal to the threshold capillary pressure ($p_c = 2\sigma/r_t$) of the throat connecting these two pores. In the threshold capillary pressure, the liquid solid contact angle ($\theta$) is omitted as in the porous medium it may differ from the liquid contact angle at the solid surface. If the solid surface contact angle were used, the capillary pressure results would shift by a factor cos($\theta$). The additional uncertainty in the capillary pressure prediction arises from the nature of the gas diffusion layer which can exhibit both wetting and non-wetting characteristics. The spreading of the wetting phase has been shown to not follow the invasion percolation mechanism [33], and networks that account for micro-force balance throughout the spreading need to be utilized. The need for the micro-force approach arises from the fact that with wetting pores present, more than one pore is filled at the same time. This violates the basic invasion percolation assumption, hence a fully non-wetting medium is modeled in this study. At the interface, one pore belongs to the cluster of the invaded fluid, and the other is filled with the invading fluid. All such pairs of pores are identified, and an average capillary pressure is calculated yielding the capillary pressure in the network. The changes of ($p_c$) as a function of both ($n_L$) and ($\chi$) are investigated. We observe that the capillary pressure behaves similarly to the single-phase permeability ($K_{sp}$) with respect to both parameters. For varying ($n_L$), a constant average ($p_c$) is observed and the deviation decreases as ($n_L$) increases (see Fig. 9 for ($K_{sp}$)). Similarly, it was fond that the stopping point (from breakthrough to terminal point that represents the land width) does not influence the capillary pressure ($p_c$). This constant ($p_c$) is dependent on the type of material used for fabricating the gas diffusion layer.

The variation of ($p_c$) with the invading fluid saturation ($s$) for ($n_L = 60$) and two distinct values of the heterogeneity parameter ($\chi = 2$ and 38) is shown in Fig. 16 (results for ($\chi = 2$) are given in small inset figure), where pairs ($s$, $p_c$) are shown with symbols. In the same figure, the square symbols with error bars show averaged ($p_c$) values and the deviation in saturation increments ($\Delta s$). The capillary pressure remains essentially constant except for very low ($s$). This is attributed to the external pressures at the network inlet and outlet boundaries; these pressures

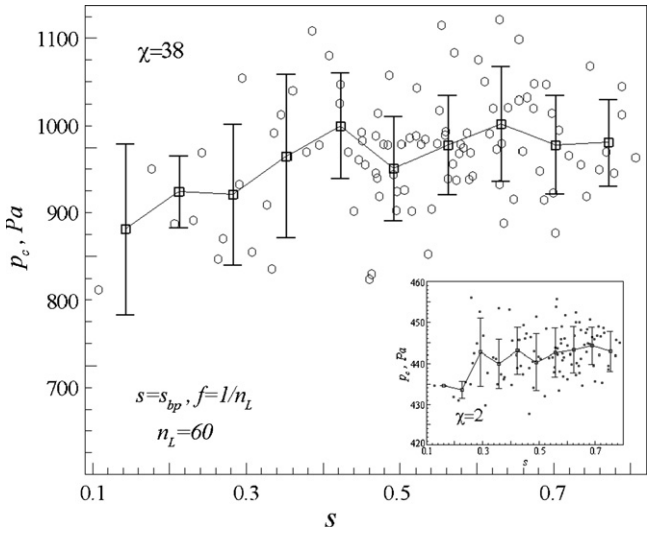


Fig. 16. Discrete random realizations of the capillary pressure for ($n_L = 60$) and ($\chi = 38$). Inset figure shows the results for ($\chi = 2$) and the same ($n_L$).

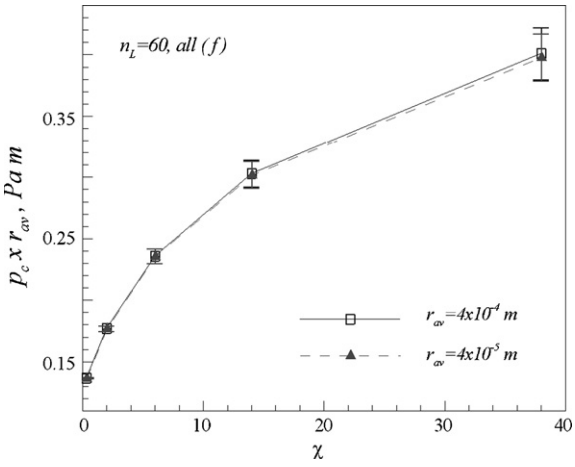


Fig. 17. Variation of averaged capillary pressure (symbols) and standard deviation (bars) as a function of heterogeneity parameter for ($n_L$ = 60) for two average pore radii values.

are maintained constant such that the flow is dominated by capillary forces, and changes of saturations are purely due to random network configurations. As the external pressure difference is not changed in the present study, the interface shape changes as a result of random configurations, but the average throat size at the interface remains the same for a set value of ($\chi$), and therefore, the capillary pressure remains constant as a function of saturation. As ($\chi$) increases, the average throat size at the interface changes, this in turn leads to an increase in ($p_c$) as shown in Fig. 17. Two types of symbols (open and full) represent the network results for two different networks ($r_{av}$, $l$) investigated. Scaling the results by ($r_{av}$), the capillary pressure results presented in the form ($p_c \times r_{av}$) are independent on value ($r_{av}$). The finding that ($p_c \sim s$) is constant should not be confused with ($p_c \sim s$) curves obtained by varying the external pressure difference [39,40], even though almost constant values of ($p_c$) were obtained in the middle of the ($p_c \sim s$) curves. When the external pressure difference is changed (e.g. increasing the current density), the capillary number and, consequently, the interface shape are altered, inducing a variation of ($p_c$) with ($s$). This dependence can be expressed using a Leverett type function. Conversely, in the present study the capillary number is small and constant, thus yielding constant ($p_c$).

## 5. Conclusions

A discrete capillary network model that uses an algorithm accounting for invasion percolation with trapping was developed and used to investigate the multiphase flow in porous media. Numerical simulations were conducted to analyze the behavior of two key parameters: relative permeability and capillary pressure, and their dependence on network size ($n_L$) and network heterogeneity ($\chi$). The relative permeability decreases as ($n_L$) increases, but in contrast with the single-phase permeability, it is found to increase with increasing network heterogeneity ($\chi$). This stems from the fact that the throats with the largest radii are preferably invaded, resulting in higher flow rates of the invading phase through the network. The relative permeability is found to remain constant for low saturation, and to follow a power law for higher saturations. The power law exponent does not depend on ($n_L$), ($\chi$) and stopping point ($f$) and approximately equal to ($n = 2.4$). However, the constant ($B$) in the relative permeability power law depends on ($n_L$) and ($\chi$) suggesting that the relative permeability needs to be corrected for the influence of the land width (included in parameters ($n_L$)). The simulations also suggest that for intermediate saturations (0.2–0.8) the capillary pressure remains constant for varying ($n_L$) and ($f$). This is attributed to the fact that for a given external pressure, the interface shape varies, but the average throat size at the interface remains the same. Both the relative permeability and capillary pressure depend on the heterogeneity ($\chi$) which characterizes a given porous medium/GDL. Finally, the scaling parameters for the relative permeability and the capillary pressure are determined and using these scales both ($k_{r,i}$) and ($p_c$) are shown to reduce to the same dependence irrespective of the network ($r_{av}$, $l$), provided that the heterogeneity ($\chi$) is kept constant. This allows convenient extension of the results to recover parameters for porous media having different physical scales without requiring additional simulations.

## References

[1] K. Tüber, D. Pocza, C. Hebling, J. Power Sources 124 (2003) 403–414.
[2] J.H. Nam, M. Kaviany, Int. J. Heat Mass Transfer 46 (2003) 4595–4611.
[3] N. Pekula, K. Heller, P.A. Chuang, A. Turhan, M.M. Mench, J.S. Brenizer, K. Ünlü, Nucl. Instrum. Methods Phys. 542 (2005) 134–141.
[4] S. Litster, D. Sinton, N. Djilali, J. Power Sources 154 (2006) 95–105.
[5] A. Bazylak, D. Sinton, Z.-S. Liu, N. Djilali, J. Power Sources 163 (2007) 784–792.
[6] S. Litster, N. Djilali, Transport Phenomena in Fuel Cells, WIT Press, Southampton, UK, 2005, pp. 175–213 (Chapter 5).
[7] T. Berning, N. Djilali, J. Electrochem. Soc. 150 (2003) A1589–A1698.
[8] Z.H. Wang, C.Y. Wang, K.S. Chen, J. Power Sources 94 (2001) 40–50.
[9] S. Mazumder, J.V. Cole, J. Electrochem. Soc. 150 (2003) A1503–A1509.
[10] S. Whitaker, Advances in Heat Transfer, vol. 13, Academic Press, New York, 1977.
[11] I. Fatt, Trans. AIME 207 (1956) 144–159.
[12] J. Koplik, J. Fluid Mech. 119 (1982) 219–247.
[13] J.B. Laurindo, M. Prat, Chem. Eng. Sci. 51 (1996) 5171–5185.
[14] M. Prat, Int. J. Multiphase Flow 19 (1993) 691–704.
[15] C. Satik, Y.C. Yortsos, ASME J. Heat Transfer 118 (1995) 455–462.
[16] X. Li, Y.C. Yortsos, AIChE J. 41 (1995) 214–222.
[17] S.C. Nowicki, H.T. Davis, L.E. Scriven, Drying Technol. 10 (1992) 925–946.
[18] V.N. Burganos, A.C. Payatakes, Chem. Eng. Sci. 47 (1992) 1383–1400.
[19] K.S. Sorbie, P.J. Clifford, Chem. Eng. Sci. 46 (1991) 2525–2542.
[20] J. Koplik, S. Redner, D. Wilkinson, Phys. Rev. A 37 (1988) 2619–2636.
[21] M. Fourar, S. Bories, R. Lenormand, P. Persoff, Water Resour. Res. 29 (1993) 3699–3708.
[22] M.A. Ioannidis, I. Chatzis, J. Colloid. Interface Sci. 229 (2000) 323–334.
[23] P. Øren, S. Bakke, O.J. Arntzen, SPE J. 3 (1998) 324–336.
[24] P.C. Reeves, M.A. Celia, Water Resour. Res. 32 (1996) 2345–2358.
[25] C.I. Bustos, P.G. Toledo, Trans. Porous Media 53 (2003) 281–315.
[26] C. Hammecker, L. Barbiero, P. Boivin, J.L. Maeght, E.H.B. Diaw, Trans. Porous Media 54 (2004) 193–219.
[27] K.A. Culligan, D. Wildenschild, B.S.B. Christensen, W.G. Gray, M.L. Rivers, A.F.B. Tompson, Water Resour. Res. 40 (2004) W12413.
[28] J.Y. Arns, V. Robins, A.P. Sheppard, R.M. Sok, W.V. Pinczewski, M.A. Knackstedt, Trans. Porous Media 55 (2004) 21–46.

[29] R. Lenormand, E. Touboul, C. Zarcone, J. Fluid Mech. 189 (1988) 165–187.
[30] R. Lenormand, C. Zarcone, Phys. Rev. Lett. 54 (1985) 2226–2229.
[31] D. Wilkinson, J.F. Willemsen, J. Phys. A 16 (1983) 3365–3376.
[32] M. Prat, Chem. Eng. J. 86 (2002) 153–164.
[33] M. Blunt, M.J. King, H. Scher, Phys. Rev. A 46 (1992) 7680–7699.
[34] S.-H. Ji, K.-K. Lee, Y.-C. Park, Trans. Porous Media 55 (2004) 153–168.
[35] L.D. Landau, E.M. Lifshitz, Electrodynamics of Continuous Media, Pergamon Press, Oxford, 1960.
[36] A. De, Wit, Phys. Fluids 7 (1995) 2553–2562.
[37] A.J. Katz, A.H. Thompson, Phys. Rev. B 34 (1986) 8179–8181.
[38] G.N. Constantinides, A.C. Payatakes, AIChE J. 42 (1996) 369–382.
[39] R.J. Held, M.A. Celia, Adv. Water Resour. 24 (2001) 325–343.
[40] H.N. Man, X.D. Jing, Trans. Porous Media 41 (2000) 263–286.